Separation and Purification Technology 327 (2023) 124967

Contents lists available at ScienceDirect

Separation and Purification Technology

journal homepage: www.elsevier.com/locate/seppur

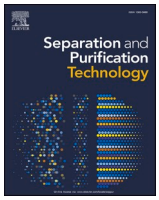

Customized pore fluorination in a microporous metal-organic framework for efficient ethane/ethylene separation

Hong-Xiang Nie [a], Mei-Hui Yu [a], Qiang Gao [b,*], Rajamani Krishna [c], Ze Chang [a,*]

[a] School of Materials Science and Engineering, National Institute for Advanced Materials, Nankai University, Tianjin 300350, China
[b] College of Environmental and Chemical Engineering, Jiangsu University of Science and Technology, Zhenjiang 212100, China
[c] Van't Hoff Institute for Molecular Sciences, University of Amsterdam, The Netherlands

ARTICLE INFO

Keywords:
Metal-organic frameworks
Ethane/ethylene separation
Ethylene purification
Fluorination of pores

ABSTRACT

High efficiency and energy-saving separation of C_2H_6/C_2H_4 mixtures to product high purity C_2H_4 is vital and very meaningful industrial task. However, it remains a formidable challenge to fabricate high-performance adsorbents with simultaneous high C_2H_6 uptake and moderate adsorption enthalpy. Here, we reported a microporous MOF (**NKU-0821**) with suitable aperture size and F atoms functional pore surface, which can capture efficiently C_2H_6 from C_2H_6/C_2H_4 mixture. Single-component adsorption experiments show that **NKU-0821a** (activated **NKU-0821**) exhibits preferred C_2H_6 uptake at the full-pressure region than C_2H_4. The corresponding C_2H_6 adsorption enthalpy of **NKU-0821a** is 27.3 kJ mol^{-1}, which is lower than most famous C_2H_6-selective MOFs. The calculation of IAST selectivity and breakthrough experiments have shown **NKU-0821a** can effectively separate C_2H_6/C_2H_4 mixture under simulated industrial conditions. Moreover, GCMC simulations revealed the key role of fluorous surface.

1. Introduction

Ethylene (C_2H_4), as one of the top-drawer chemical feedstocks in the world with a spectacular annual outputs exceeded 180 million tons in 2019, currently mainly used to produce important commodity chemicals such as polyethylene [1,2]. In the industry, the formation of C_2H_4 predominantly from the steam cracking of ethane (C_2H_6) or naphtha. However, as a substantial impurity, C_2H_6 will also usually appear in the above process [3–5]. In order to meet the purity requirements of polymer-grade C_2H_4 (≥99.95%) for industrial production, the effective elimination of coexisting C_2H_6 becomes imperative. Attribute to their exceeding similar physical and chemical properties (boiling point: 184.5 K for C_2H_6; 169.4 K for C_2H_4) and structural features (molecular size: 3.81 × 4.08 × 4.82 $Å^3$ for C_2H_6, 3.28 × 4.18 × 4.84 $Å^3$ for C_2H_4), the separation of C_2H_6/C_2H_4 mixture for C_2H_4 depuration is very challenging [6–8]. In actual industrial operation, the high-purity C_2H_4 can be obtained with the aide of high-cost and energy-intensive cryogenic distillation process [9]. Both industry and academia are eager to develop alternative technologies to accomplish the aim of green and low-budget separation pathway. Owing to the advantage of energy-saving and environment-friendly, adsorption separation with porous solid materials has aroused great interest in the related fields [10,11]. But, upon most occasions, already developed traditional porous materials, such as zeolites, clay, and porous carbons, et.al, suffer from the low adsorption capacity and poor separation selectivity, which mainly be subjected to their limited structural components and characteristics that are difficult to functionalize [12,13].

Metal-organic frameworks (MOFs), as one kind of novel crystalline porous materials, have shown great application potential in many areas, such as gas adsorption and separation [14–16], heterogeneous catalysis [17–19], fluorescent sensing [20–22], drug delivery/biomedicine et.al [23,24]. On account of their large specific surface area, high porosity, highly controllable pore size and surface microenvironment, MOFs were also evolved as adsorbents for C_2H_6/C_2H_4 separation. The very beginning, a large numbers of C_2H_4-selective MOFs have been constructed based on π-complexing or size sieving strategies [25–28], which demonstrated efficient separation performance. However, there are also many significant disadvantages for this type of adsorbents. For instance, additional desorption steps are required to produce pure C_2H_4, which usually contains a purge gas and high temperatures or vacuum conditions. By contrast, C_2H_6-selective adsorbents are considered to be more efficient, which can directly harvest high-purity C_2H_4 in one step. Up to now, although numerous progress has been made to develop C_2H_6-selective MOF for C_2H_6/C_2H_4 separation [29–31], it is still challenging to

* Corresponding authors.
E-mail addresses: gaoq@just.edu.cn (Q. Gao), changze@nankai.edu.cn (Z. Chang).

https://doi.org/10.1016/j.seppur.2023.124967
Received 14 July 2023; Received in revised form 20 August 2023; Accepted 28 August 2023
Available online 1 September 2023

simultaneously achieve both high C_2H_6 capacity and low adsorption enthalpy.

Owing to the slightly bigger size and more H atoms, C_2H_6 is expected to form more and stronger bonds with the high-polarize pore walls functionalized special sites. Theoretically, polar F atoms with appropriate distribution can serve as strong binding sites for C_2H_6 through hydrogen bonds, resulting in notably improved C_2H_6/C_2H_4 selectivity. The suppose has been confirmed by our recent work and some related previous reports [32–35]. For further exploration, herein, adopting terephthalic acid containing fluoride pyridine unit (namely, H_2FPTC = (5-fluoropyridin-3-yl)terephthalic acid), we constructed a unique Zn-based MOF {[Zn(FPTC)]·$(DMF)_{3.5}$·$(H_2O)_n$} (**NKU-0821**). **NKU-0821** has the fluorinated surface environment with proper pore size, which exhibit suitable confinement effect and higher affinity for C_2H_6 than C_2H_4. Gas adsorption experiments show that **NKU-0821a** (activated **NKU-0821**) exhibits comparatively high adsorption capacity and low adsorption enthalpy for C_2H_6. The effective C_2H_6/C_2H_4 separation ability of **NKU-0821a** was verified by breakthrough experiments. And, the GCMC simulations further reveal the underlying adsorption mechanism. All results of experiments and simulations show that **NKU-0821a** is a promising C_2H_6-selective adsorbent for C_2H_4 purification under real working conditions.

2. Materials and methods

2.1. Materials and characterization

All chemicals and reagents were purchased from commercial suppliers and used without further purification. Powder X-ray diffraction (PXRD) was measured on a Rigaku Miniflex 600 with Cu Kα radiation (λ = 1.5425 Å) under air conditions. The simulated PXRD pattern was calculated using Mercury software from the data of single-crystal X-ray diffraction structure. Variable-temperature PXRD were performed on a Rigaku SmartLab diffractometer equipped with a TTK 600 chamber to control the temperature. Thermogravimetric analysis (TGA) was recorded on a Rigaku standard thermogravimetry–differential thermal analysis (TG-DTA) analyzer utilizing an empty and clean Al_2O_3 crucible as reference (heating rate = 10 °C min^{-1} in Ar atmosphere).

2.2. Preparation of NKU-0821

A solvothermal reaction of mixtures about $Zn(NO_3)_2·6H_2O$ (29.8 mg, 0.1 mmol) and H_2FPTC (24.3 mg, 0.1 mmol) in 4 mL DMF were sealed in a 20 mL screw-capped vial in an oven at 100 °C for 3 days, and faint yellow block crystals of **NKU-0821** were first time synthesized in 81 % yield based on the H_2FPTC ligand. (Figure S1) Selected IR data (KBr, cm^{-1}): 416.76(w), 540.50(w), 773.788(m), 886.15(m), 1089.55 (s), 1705.44 (s) (Figure S2).

2.3. Single-crystal X-ray diffraction study

The single crystal intensity data of **NKU-0821** was conducted at 100 K on a Bruker-AXS SMART CCD area detector diffractometer under Cu Kα radiation (λ = 0.71073 Å) with ω rotation scans at a scan width of 0.3°. The structure was solved with direct methods of *SHELXT* and refined using *SHELXL* on *OLEX2* software suite [36–38]. Partial lattice solvent molecules in the structures of complexes **NKU-0821** were disordered and could not be modeled properly. Therefore, the intensity contributions from the lattice guests were removed by using the *SQUEEZE* operation of *PLATON* [39]. The formulas were given by integrating the crystal structure, elemental microanalysis, IR, and TGA. The details of crystallographic data of **NKU-0821** are provided in Table S1, and the CCDC reference number for **NKU-0821** is 2280924.

2.4. Gas sorption measurement

Before the sorption measurement, the sample of NKU-0821 was soaked in anhydrous acetone for 3 days to exchange solvent molecules in the channels. The degas procedure for the acetone-exchanged NKU-0821 was conducted at 120 °C under a high vacuum (<10^{-5} Torr) overnight and led to the formation of a completely activated sample. About 100 mg of the desolvated sample was used for the entire sorption measurements. The N_2 sorption isotherm measurement was carried out using a Micrometrics ASAP 2460 M volumetric gas adsorption analyzer at 77 K in a liquid-nitrogen bath. The C_2H_6 and C_2H_4 sorption isotherms at 273 and 298 K were recorded by a Micrometrics ASAP 2020 M volumetric gas adsorption analyzer.

2.5. Breakthrough experiments

The breakthrough experiments of C_2H_6/C_2H_4 were performed on a homemade fixed bed. 3.28 g **NKU-0821a** Sample was packaged in a transparent quartz column with 120 mm in length and 10 mm in inner diameter. The gas flows of C_2H_6/C_2H_4 mixtures were regulated by a mass flow controller, and the out-of-column gas flow was detected by gas chromatography (GC) with a TCD detector. Before breakthrough experiment, the column was purged with He for 12 h at 100 °C. In continuous cycling experiments, samples were regenerated by desorption with He purging at 373 K for 120 min.

2.6. Grand Canonical Monte Carlo (GCMC) simulations

The GCMC simulations were carried out for the adsorption mechanism study on Material Studio. The framework of **NKU-0821a** and gas molecules were regarded as rigid bodies. The optimal adsorption sites were simulated under 298 K and 1.0 bar by the fixed loading task and Metropolis method. The loading steps, equilibration steps and the production steps were all set to 1.0×10^7. The saturation/maximum uptakes were modeled at 298 K using the fixed pressure task with 1.0×10^7 equilibration steps, followed by 1.0×10^7 production steps for calculating the ensemble averages. The gas-skeleton interaction and the gas–gas interaction were characterized by the standard universal force field (UFF). The atomic partial charges of the host skeleton of **NKU-0821a** were used for Q_{eq} method. The guest gas molecules were optimized using the method of $DMol^3$ and adopted the B3LYP fitted charge. The cut-off radius used for the Lennard–Jones interactions is 18.5 Å [40,41].

3. Results and discussion

3.1. Crystal structural description

Single-crystal X-ray structure analysis revealed that **NKU-0821** crystallizes in the monoclinic space group $P2_1/n$. There are three independent Zn^{2+} ions and three $FPTC^{2-}$ ligands in the asymmetric unit (Figure S2). Two kinds of binuclear Zn_2 secondary building units (SBUs) can be found in the structure of **NKU-0821**. One Zn SBU displays a tetragonal pyramid geometry connected by two Zn ions, four carboxyl groups of four different $FPTC^{2-}$ ligands and two N atoms from two different $FPTC^{2-}$ ligands, all of which generate a paddle-wheel $[Zn_2(COO)_4N_2]$ cluster. Another dinuclear SBU exhibits distorted tetragonal pyramid geometries defined by four carboxyl groups and two N atoms from four six $FPTC^{2-}$ ligands. The neighboring two SBUs are connected by $FPTC^{2-}$ to give an interesting 2D supramolecular layer (Figure S3, S4). Further, these 2D layers are joined together by pyridine units to generate a 3D pillared-layer framework. The topological type of the original 2D supramolecular network has also evolved to a rare 3,6-connected topology network with a point symbol of $\{4^2.6\}_4\{4^3\}_2\{4^4.6^2.8^6.10^3\}\{4^5.6^4.8^6\}_2$ (Figure S5). As shown in Fig. 1, there is one class of representative quadrangular 1D channel about 13.5

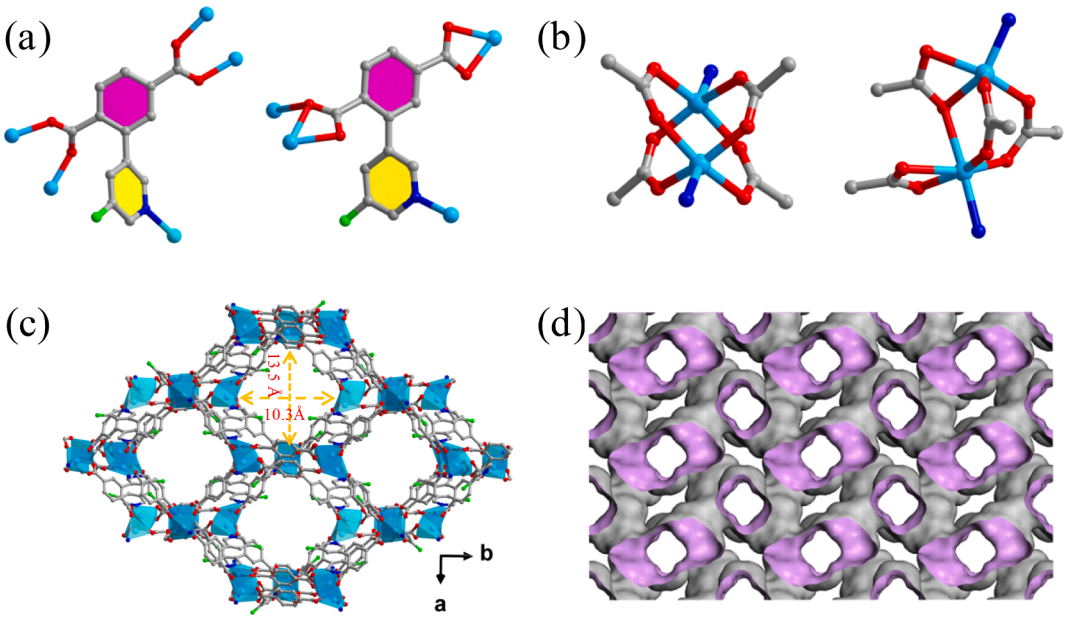

Fig. 1. X-ray single crystal structure of **NKU-0821**, indicating (a) the coordination model of each organic ligand $FPTC^{2-}$ and (b) the coordination environments of Zn (II) ions in two type of binuclear zinc SBUs. The pore structures (c) and Connolly surface void spaces (d) of **NKU-0821** view along the *c* axis.

$\times$ 10.3 $Å^2$ along *c* axis in **NKU-0821**. And the pore surface modified by free F atoms is supposed to afford specific recognition sites for alkane. Theoretical calculation from *PLATON* indicates that the total accessible porosity is 52.0 % in **NKU-0821** after ignoring the guest solvent molecules.

3.2. Crystal purity and stability analysis

Before the adsorption property studies, the phase purity of **NKU-0821** was examined whereby PXRD experiment. As indicated in Figure S6, the experimental PXRD pattern of as-synthesized **NKU-0821** agrees well with the simulated one based on the single crystal data, indicating the high phase purity of the synthesized sample and framework stability after activating of **NKU-0821** (Figure S7). Thermogravimetric analysis experiments under an Ar atmosphere were carried out to study the thermal stability of the activated sample, showing almost no mass change before 380 °C because the solvent molecules in the lattice had been completely released in the pores. Then, the curve decreased sharply from 380 to 560 °C due to the decomposition of framework (Figure S8). The resuelts of variable temperature XRD showed that **NKU-0821** remained structurally stable up to 400 ℃, which is consistent with the thermogravimetric curve (Figure S9). Concurrently, the PXRD patterns of soaked samples in common solvents manifested its good stability (Figure S10).

3.3. Gas adsorption properties of NKU-0821a

To assess the pore textural properties of **NKU-0821a**, the N_2 sorption experiment at 77 K was measured. An apparent type I isotherm of N_2 exhibited a fully reversible behavior, corroborating the permanent porosity and microporous nature. The adsorption capacity of **NKU-0821a** ascends a plateau at around $P/P_0 = 0.01$ and the homologous specific pore volume of 0.52 $cm^3\ g^{-1}$ is calculated when the saturation uptake reached 337.73 $cm^3\ g^{-1}$. The measured pore size distribution curves based on the density-functional theory method show the main pore sizes of 7.3 and 9.3 Å, which is consistent with the results obtained by single-crystal structure analysis. The Brunauer-Emmett-Teller (BET) and Langmuir surface area reach 962.27 m^2/g and 1449.43 m^2/g for **NKU-0821a**.

Motivated by the excellent stability and special pore structure, the hydrocarbon gases adsorption and separation behavior of **NKU-0821a** was explored. First, single component adsorption isotherms of **NKU-0821a** for C_2H_6 and C_2H_4 were measured with pressure of up 1 bar at 273 and 298 K, respectively. As exhibited in Fig. 2b and 2c, **NKU-0821a** adsorbed more C_2H_6 than C_2H_4 in the full pressure range, and the uptakes can reach to 122.31/96.07 $cm^3\ g^{-1}$ and 115.39/82.27 $cm^3\ g^{-1}$ at 273/298 K and 1 bar, respectively. The results manifested that **NKU-0821a** demonstrated great potential for C_2H_6/C_2H_4 separation. Further, the coverage-dependent adsorption enthalpy (Q_{st}) for the **NKU-0821a**, a quantitative measurement of the binding affinity, was calculated by fitting adsorption isotherms at 273 and 298 K using the virial equation. The fitting parameters are shown in Figures S10 and S11. As depicted in Fig. 2d, the zero coverage Q_{st} values of C_2H_6 (27.3 kJ mol^{-1}) higher than those of C_2H_4 (25.0 kJ mol^{-1}), indicating that **NKU-0821a** has a stronger thermodynamic affinity toward C_2H_6 than C_2H_4. It is lower than many MOF reported so far, which is conducive to the regeneration of adsorbent. In short, the adsorption capacity of C_2H_6 (5.15 mmol g^{-1} at 298 K and 1 bar) and Q_{st} is modest in reported MOFs materials, well than or comparable to many well-known similar materials, such as UiO-67-$(NH_2)_2$ (4.32 mmol g^{-1} and 26.5 kJ mol^{-1}) [3], UiO-67-BN (3.9 mmol g^{-1} and 24.6 kJ mol^{-1}) [29], NUM-7 (2.85 mmol g^{-1} and 35.8 kJ·mol^{-1}) [42], and $Cu(Qc)_2$ (1.85 mmol g^{-1} and 28.8 kJ mol^{-1}) [7], CAU-11 (1.81 mmol g^{-1} and 31.0 kJ mol^{-1}) [43], BIF-108-Zn (2.8 mmol g^{-1} and 22.5 kJ mol^{-1}) [44], NKMOF-8-Me (4.67 mmol g^{-1} and 38.4 kJ mol^{-1}) [4], Tb-MOF-76 (NH_2) (3.03 mmol g^{-1} and 32.8 kJ mol^{-1}) [45], Zr-Me-PDI (3.9 mmol g^{-1} and ≈16.5 kJ mol^{-1}) [46] and HOF-NBDA (39.8 mmol g^{-1} and 23.5 kJ mol^{-1}) [47] (Fig. 3a). The results manifested that **NKU-0821a** demonstrated great potential for C_2H_6/C_2H_4 separation.

3.4. Gas separation properties of NKU-0821a

Due to the significant differences in adsorption capacity and heat of adsorption between C_2H_6 and C_2H_4, we conclude that **NKU-0821a** may be a promising candidate for efficient purification of C_2H_4 in C_2H_4/C_2H_6 mixtures. In order to evaluate the separation ability of **NKU-0821a**, the separation performance of binary C_2H_6/C_2H_4 gas mixtures at two different temperatures was predicted by using the ideal adsorbed solution theory (IAST). As shown in Fig. 3b, **NKU-0821a** exhibited moderate C_2H_6/C_2H_4 selectivities about 1.791–1.664 or 1.783–1.649 for 10/90 or

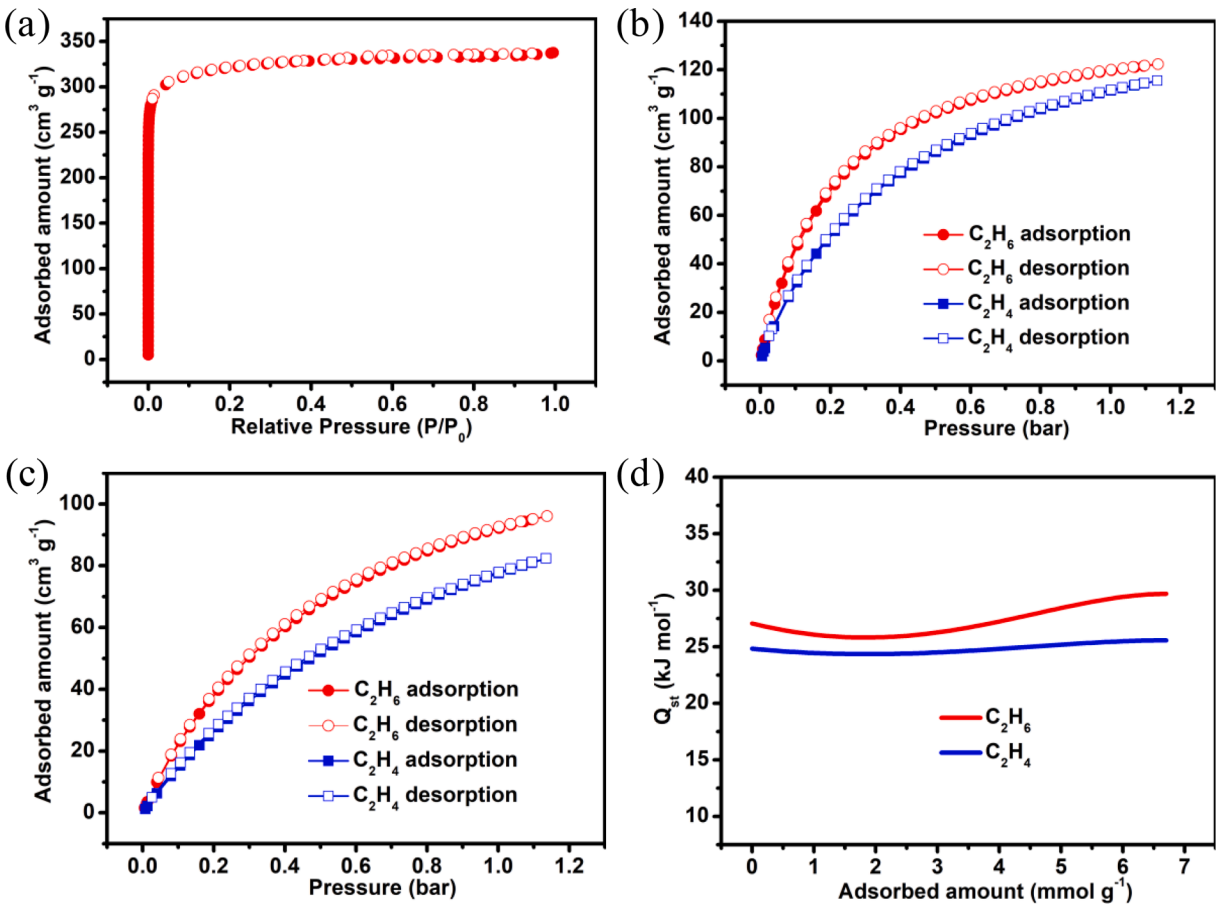

Fig. 2. (a) N_2 sorption isotherm at 77 K and pore size distribution of **NKU-0821a**. Single-component gas isotherms for C_2H_6 and C_2H_4 of **NKU-0821a** at (b) 273 and (c) 298 K. (d) Isosteric enthalpy of adsorption (Q_{st}) of C_2H_6 and C_2H_4 in **NKU-0821a**.

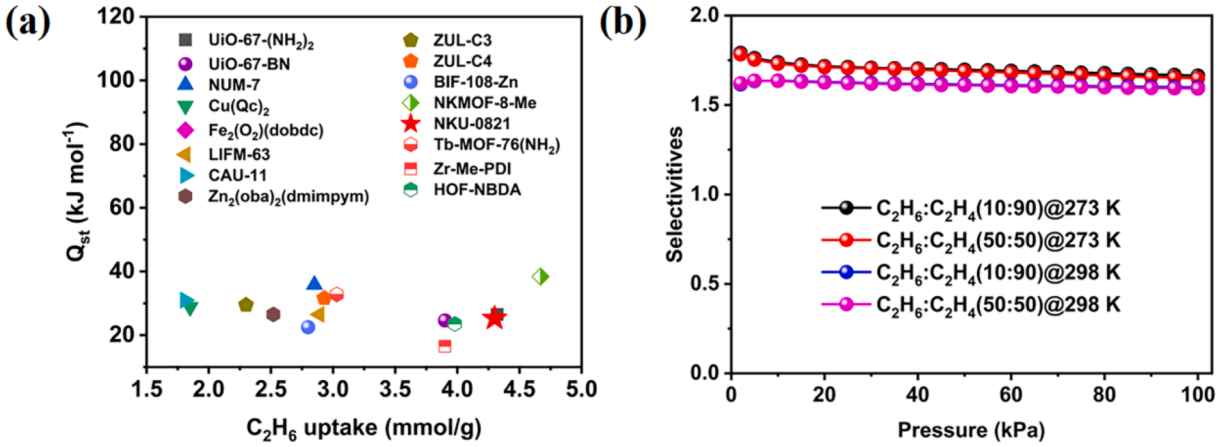

Fig. 3. Comparison of C_2H_6 uptake and Q_{st} of **NKU-0821a** and other similar materials at 298 K. (b) The C_2H_6/C_2H_4 selectivities of **NKU-0821a** predicted from IAST at 273 K and 298 K.

50/50 C_2H_6/C_2H_4 mixture at 273 K. And **NKU-0821a** exhibited weaker selectivities with values of 1.616–1.598 (10/90) and 1.621–1.592 (50/50) at 298 K, respectively.

To test the recycling adsorption performance of **NKU-0821a**, five cycles of C_2H_6 and C_2H_4 adsorption/desorption were performed at 298 K and 1 bar. As shown in Fig. 4a and 4b, the ability to adsorb C_2H_6 and C_2H_4 after the cycling experiment almost on changes, proving excellent reproducibility of **NKU-0821a**. The gas separation under dynamic process is very important in practical application. To verify the feasibility of the separation effect of **NKU-0821a** for C_2H_4 from C_2H_6/C_2H_4 mixture, The transient breakthrough simulation for 50/50 C_2H_6/C_2H_4 mixtures on **NKU-0821a** was carried out at 298 K and 100 kPa. As shown in Figure S16, C_2H_4 gas as the effluent firstly flows out and of the fixed bed and C_2H_6 passed through some time later. To verify the feasibility of the separation effect of **NKU-0821a** for C_2H_4 from C_2H_6/C_2H_4 mixture, we conducted breakthrough experiment to simulate the industrial conditions with the feed gas of C_2H_6/C_2H_4, where the gas volume ratio is 1/1 (v/v) flowed over a packed column of activated **NKU-0821** with a total

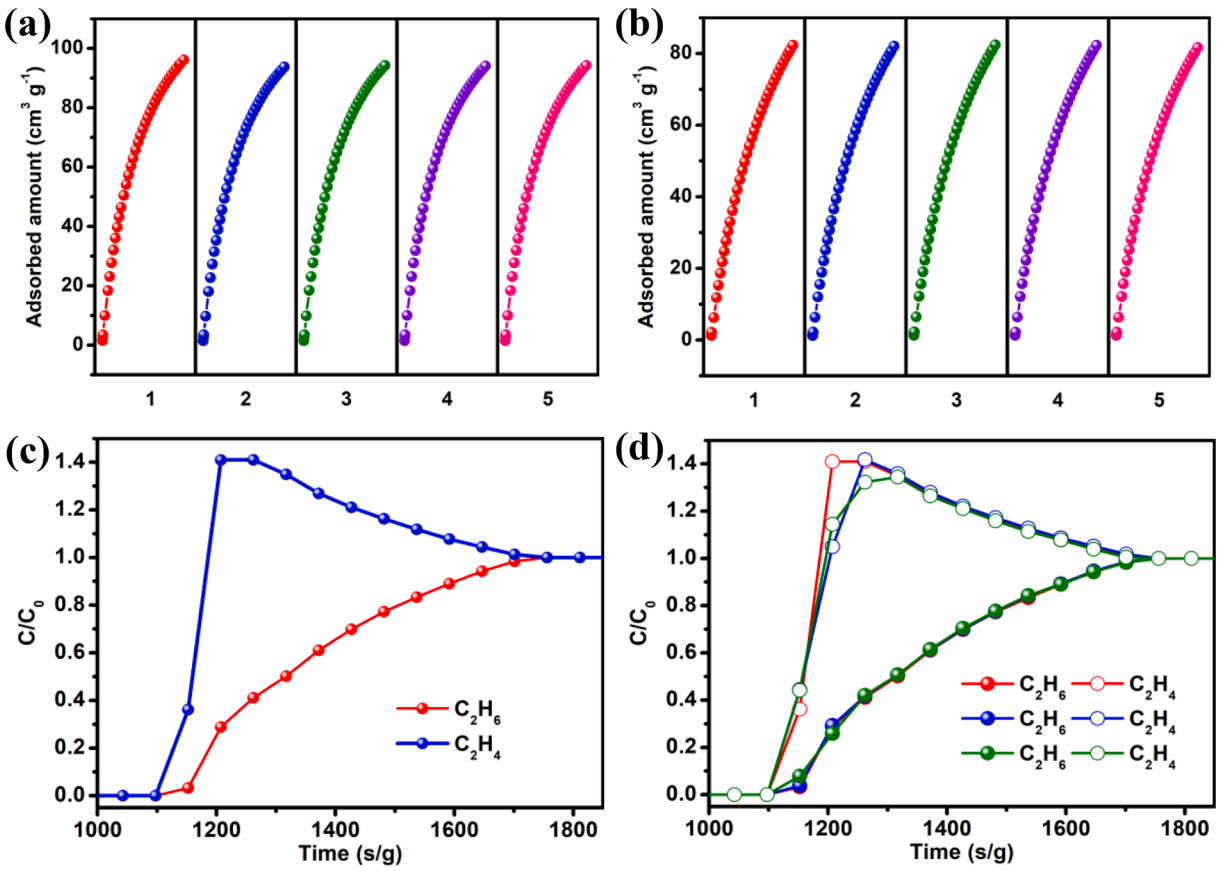

Fig. 4. Five cycles adsorption curve of C_2H_6 (a) and C_2H_4 (b) at 298 K. (c) The dynamic breakthrough curves for mixture gases of C_2H_6/C_2H_4 (50:50, v/v) at 298 K and 1 bar for **NKU-0821a**. (d) Cyclic curves of breakthrough experiments (first: red; second: blue; third: green). (For interpretation of the references to colour in this figure legend, the reader is referred to the web version of this article.)

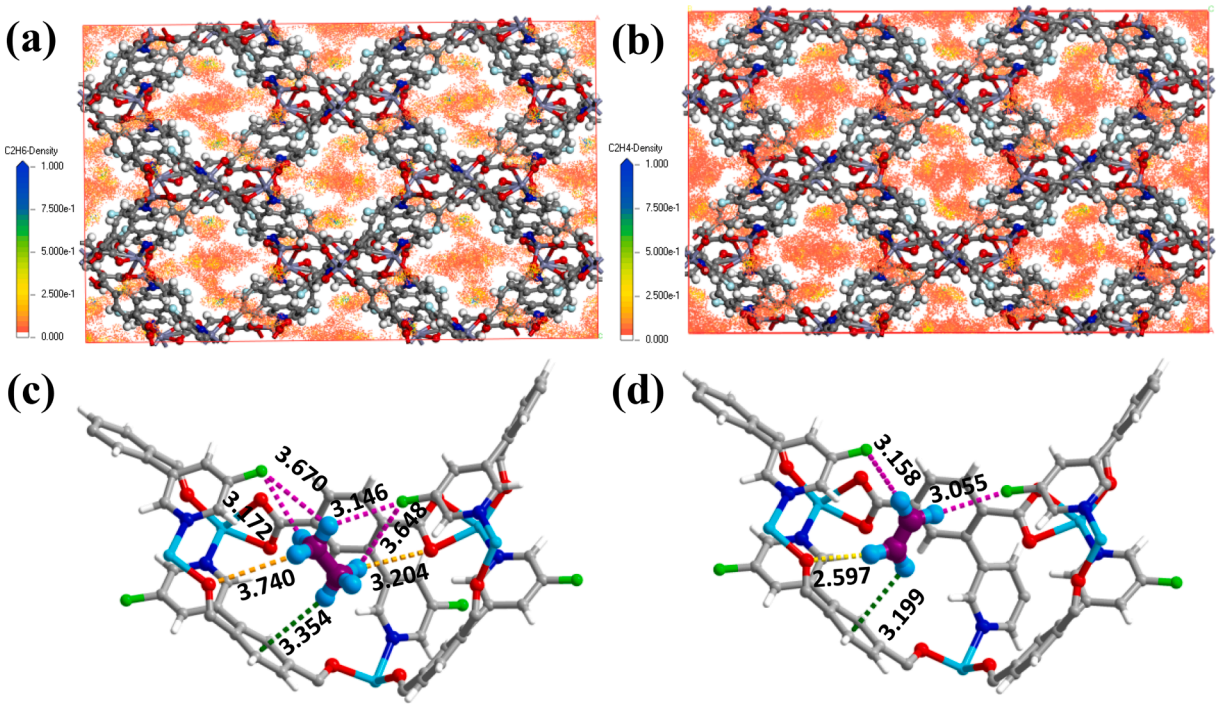

Fig. 5. GCMC simulated density distributions of C_2H_6 (a) and C_2H_4 (b) in **NKU-0821a** at 298 K and 1 bar, where the label ranges is from 0 to 1. GCMC simulated preferential adsorption sites of C_2H_6 (c) and C_2H_4 (d) in **NKU-0821a** at 298 K and 1 bar.

inlet rate of 5.0 mL min^{-1} at operation temperature of 298 K and pressure 1 bar. When the mixed gas is passed through a packed bed, C_2H_4 first flowed through and was detected in the outlet effluent gas. After that, C_2H_6 reached its breakthrough point. The practical C_2H_4 capture productivity under dynamic condition, calculated on the basis of the measured breakthrough curve for the full process, was attained to 28.8 cm^3 g^{-1}. It worth noting that the purity of ourlet C_2H_4 is only 92 %. In our viewpoint, it maybe attribuatable to intra-crystalline diffusion influences. The good match between result of transient breakthrough simulation and that from experimental confirmed the above inference. Furthermore, we compared **NKU-0821a** after breakthrough testing with synthetic and simulated XRD, which confirmed the good stability of the **NKU-0821a** (Figure S17).

3.5. GCMC simulation

In order to probe into the sorption and separation mechanisms of C_2H_6-selected performance than C_2H_4 in **NKU-0821a**, theoretical GCMC simulation were further carried out to calculate the preferential interaction sites and the density distributions at 298 K and 1 bar. As shown in Fig. 5, the calculated preferential binding sites of C_2H_6 and C_2H_4 are all located in the central region of four diagonal positions of rhombic orifice region. C_2H_6 forms four more powerful C-H···F hydrogen interactions (C-H···F 3.146——3.740 Å) with the –CH units on the C_2H_6 and F atoms on pyridine rings. At the same time, another C-H···π interaction (3.354 Å) originating from the –CH units between one end of C_2H_6 and pyridine ring is found. Except for the above-mentioned interactions, two C-H···O hydrogen bond interactions were also detected between H atoms of C_2H_6 and coordinated O atoms in carboxylic acid group of benzene ring. The approaching distance of hydrogen bond interactions for C_2H_6 is 3.204 and 3.745 Å. On the contrary, the adsorbed C_2H_4 in **NKU-0821a** is arranged in the middle of two C-H···F hydrogen interactions (3.055 and 3.158 Å) from pyridine rings, one C-H···π interactions (3.199 Å) from benzene ring, and one C-H···O hydrogen bond interactions (2.597 Å) from carboxylic acid O atom. Based on the above analysis, it can be seen that C_2H_6 has a stronger interaction with the framework of **NKU-0821a** than C_2H_4, which is in good agreement with the calculations of adsorption and adsorptive separation experiments.

4. Conclusion

In summary, we successfully construct a fluorinated MOF **NKU-0821** with highly porous volumes by employing a F group modified pyridyldicarboxylate ligands. The single-component adsorption isotherms revealed that **NKU-0821a** could adsorb more C_2H_6 than C_2H_4 in the whole pressure region. Ascribe to the suitable pore sizes and unique pore environment, it is clear that **NKU-0821a** shows comparative advantage in C_2H_6 adsorption capacity and adsorption enthalpy among the C_2H_6-selective MOFs. This work provides valuable insights for construction of high-performance porous materials which are expected to be applied in practical industrial processes to address separation challenges.

CRediT authorship contribution statement

Hong-Xiang Nie: Data curation, Visualization, Investigation, Writing – original draft. **Mei-Hui Yu:** Methodology, Software, Formal analysis, Visualization. **Qiang Gao:** Supervision, Conceptualization, Funding acquisition, Writing – review & editing. **Rajamani Krishna:** . **Ze Chang:** Supervision, Conceptualization, Project administration, Funding acquisition, Resources, Writing – review & editing.

Declaration of Competing Interest

The authors declare that they have no known competing financial interests or personal relationships that could have appeared to influence the work reported in this paper.

Data availability

Data will be made available on request.

Acknowledgements

This work was financially supported by National Natural Science Foundation of China (22005153, 22001098), Haihe Laboratory of Sustainable Chemical Transformations (YYJC202101) and the Ph.D. Candidate Research Innovation Fund of NKU School of Materials Science and Engineering.

Appendix A. Supplementary data

Supplementary data to this article can be found online at https://doi.org/10.1016/j.seppur.2023.124967.

References

[1] Q. Ding, Z. Zhang, Y. Liu, K. Chai, R. Krishna, S. Zhang, One-Step Ethylene Purification from Ternary Mixtures in a Metal-Organic Framework with Customized Pore Chemistry and Shape, Angew. Chem. Int. Ed. 61 (2022) e202208134.
[2] B. Zhu, J.-W. Cao, S. Mukherjee, T. Pham, T. Zhang, T. Wang, X. Jiang, K. A. Forrest, M.J. Zaworotko, K.-J. Chen, Pore Engineering for One-Step Ethylene Purification from a Three-Component Hydrocarbon Mixture, J. Am. Chem. Soc. 143 (2021) 1485–1492.
[3] X.-W. Gu, J.-X. Wang, E. Wu, H. Wu, W. Zhou, G. Qian, B. Chen, B. Li, Immobilization of Lewis Basic Sites into a Stable Ethane-Selective MOF Enabling One-Step Separation of Ethylene from a Ternary Mixture, J. Am. Chem. Soc. 144 (2022) 2614–2623.
[4] S. Geng, E. Lin, X. Li, W. Liu, T. Wang, Z. Wang, D. Sensharma, S. Darwish, Y. H. Andaloussi, T. Pham, P. Cheng, M.J. Zaworotko, Y. Chen, Z. Zhang, Scalable Room-Temperature Synthesis of Highly Robust Ethane-Selective Metal-Organic Frameworks for Efficient Ethylene Purification, J. Am. Chem. Soc. 143 (2021) 8654–8660.
[5] Y. Wang, C. Hao, W. Fan, M. Fu, X. Wang, Z. Wang, L. Zhu, Y. Li, X. Lu, F. Dai, Z. Kang, R. Wang, W. Guo, S. Hu, D. Sun, One-step Ethylene Purification from an Acetylene/Ethylene/Ethane Ternary Mixture by Cyclopentadiene Cobalt-Functionalized Metal-Organic Frameworks, Angew. Chem. Int. Ed. 60 (2021) 11350–11358.
[6] H. Zeng, X.-J. Xie, M. Xie, Y.-L. Huang, D. Luo, T. Wang, Y. Zhao, W. Lu, D. Li, Cage-Interconnected Metal-Organic Framework with Tailored Apertures for Efficient C2H6/C2H4 Separation under Humid Conditions, J. Am. Chem. Soc. 141 (2019) 20390–20396.
[7] R.-B. Lin, H. Wu, L. Li, X.-L. Tang, Z. Li, J. Gao, H. Cui, W. Zhou, B. Chen, Boosting Ethane/Ethylene Separation within Isoreticular Ultramicroporous Metal-Organic Frameworks, J. Am. Chem. Soc. 140 (2018) 12940–12946.
[8] D.S. Sholl, R.P. Lively, Seven Hemical Separations to Change the World, Nature 532 (2016) 435–437.
[9] T. Ren, M. Patel, K. Blok, Olefins from Conventional and Heavy Feedstocks: Energy Use in Steam Cracking and Alternative Processes, Energy 31 (2006) 425–451.
[10] D. Yuan, W. Lu, D. Zhao, H.-C. Zhou, Highly Stable Porous Polymer Networks with Exceptionally High Gas-Uptake Capacities, Adv. Mater. 23 (2011) 3723–3725.
[11] Y. Wang, S.B. Peh, D. Zhao, Alternatives to Cryogenic Distillation: Advanced Porous Materials in Adsorptive Light Olefin/Paraffin Separations, Small 15 (2019) 1900058.
[12] R.T. Yang, E.S. Kikkinides, New Sorbents for Olefin/paraffin Separations by Adsorption via π -complexation, AIChE Journal 41 (1995) 509–517.
[13] Y. Cheng, S.J. Datta, S. Zhou, J. Jia, O. Shekhah, M. Eddaoudi, Advances in Metal–organic Framework-based Membranes, Chem. Soc. Rev. 51 (2022) 8300–8350.
[14] R.-B. Lin, S. Xiang, H. Xing, W. Zhou, B. Chen, Exploration of Porous Metal–organic Frameworks for Gas Separation and Purification, Coord. Chem. Rev. 378 (2019) 87–103.
[15] Q. Zhang, L. Zhou, P. Liu, L. Li, S.-Q. Yang, Z.-F. Li, T.-L. Hu, Integrating Tri-mural Nanotraps into a Microporous Metal-organic Framework for C_2H_2/CO_2 and C_2H_2/C_2H_4 separation, Separation Purification Technol. 296 (2022), 121404.
[16] L. Wang, H. Huang, X. Zhang, H. Zhao, F. Li, Y. Gu, Designed Metal-organic Frameworks with Potential for Multi-component Hydrocarbon Separation, Coord. Chem. Rev. 484 (2023), 215111.
[17] A. Bavykina, N. Kolobov, I.S. Khan, J.A. Bau, A. Ramirez, J. Gascon, Metal-Organic Frameworks in Heterogeneous Catalysis: Recent Progress, New Trends, and Future Perspectives, Chem. Rev. 120 (2020) 8468–8535.
[18] L. Feng, K.-Y. Wang, X.-L. Lv, T.-H. Yan, H.-C. Zhou, Hierarchically porous metal–organic frameworks: synthetic strategies and applications, Natl. Sci. Rev. 7 (2020) 1743–1758.
[19] C.-D. Wu, M. Zhao, Incorporation of Molecular Catalysts in Metal-Organic Frameworks for Highly Efficient Heterogeneous Catalysis, Adv. Mater. 29 (2017) 1605446.

[20] C. Jia, T. He, G.-M. Wang, Zirconium-based Metal-organic Frameworks for Fluorescent Sensing, Coord. Chem. Rev. 476 (2023), 214930.
[21] Q. Xia, J. Zhang, X. Chen, C. Cheng, D. Chu, X. Tang, H. Li, Y. Cui, Synthesis, structure and property of boron-based metal–organic materials, Coord. Chem. Rev. 435 (2021) 213783.
[22] B. Wang, R.-B. Lin, Z. Zhang, S. Xiang, B. Chen, Hydrogen-Bonded Organic Frameworks as a Tunable Platform for Functional Materials, J. Am. Chem. Soc. 142 (34) (2020) 14399–14416.
[23] C. Pettinari, R. Pettinari, C. Di Nicola, A. Tombesi, S. Scuri, F. Marchetti, Antimicrobial MOFs, Coord. Chem. Rev. 446 (2021) 214121.
[24] I. Abánades Lázaro, R.S. Forgan, Application of Zirconium MOFs in Drug Delivery and Biomedicine, Coord. Chem. Rev. 380 (2019) 230–259.
[25] Z. Bao, G. Chang, H. Xing, R. Krishna, Q. Ren, B. Chen, Potential of Microporous Metal–organic Frameworks for Separation of Hydrocarbon Mixtures, Energ. Environ. Sci. 9 (12) (2016) 3612–3641.
[26] E.D. Bloch, W.L. Queen, R. Krishna, J.M. Zadrozny, C.M. Brown, J.R. Long, Hydrocarbon Separations in a Metal-Organic Framework with Open Iron(II) Coordination Sites, Science 335 (6076) (2012) 1606–1610.
[27] S. Yang, A.J. Ramirez-Cuesta, R. Newby, V. Garcia-Sakai, P. Manuel, S.K. Callear, S. I. Campbell, C.C. Tang, M. Schröder, Supramolecular Binding and Separation of Hydrocarbons within a Functionalized Porous Metal–organic Framework, Nat. Chem. 7 (2) (2015) 121–129.
[28] R.-B. Lin, L. Li, H.-L. Zhou, H. Wu, C. He, S. Li, R. Krishna, J. Li, W. Zhou, B. Chen, Molecular Sieving of Ethylene from Ethane using a Rigid Metal–organic Framework, Nat. Mater. 17 (12) (2018) 1128–1133.
[29] Y. Han, L. Meng, Y. Liu, H. Li, Z. Ji, Y. Zhou, M. Wu, Z. Han, Expanding Nonpolar Pore Surfaces in Stable Ethane-selective MOF to Boost Ethane/ethylene Separation Performance, Sep. Purif. Technol. 315 (2023) 123642.
[30] L. Li, R.-B. Lin, R. Krishna, H. Li, S. Xiang, H. Wu, J. Li, W. Zhou, B. Chen, Ethane/ethylene Separation in a Metal-organic Framework with Iron-peroxo Sites, Science 362 (6413) (2018) 443–446.
[31] Z. Heng, X.-J. Xie, M. Xie, Y.-L. Huang, D. Luo, T. Wang, Y.-F. Zhao, W.-G. Lu, D. Li, A Cage-Interconnected Metal-Organic Framework with Tailored Apertures for Efficient C_2H_6/C_2H_4 Separation under Humid Conditions, J. Am. Chem. Soc. 141 (2019) 20390–20396.
[32] L.-Z. Yang, L.-T. Yan, W.-J. Niu, Y. Feng, Q.-J. Fu, S. Zhang, Y.-H. Zhang, L.-J. Li, X. Gu, P.-C. Dai, D.-D. Liu, Q.-B. Zheng, X.-B. Zhao, Adsorption in Reversed Order of C2 Hydrocarbons on anUltramicroporous Fluorinated Metal-Organic Framework, Angew. Chem. Int. Ed. 61 (2022) e202204046.
[33] P.-T. Guo, Y.-P. Ying, M. Chang, D.-H. Liu, One Ethane-selective Metal–organic Framework with Customized Pore Size and Specific Binding Sites for Efficient Purification of Ethylene, Sep. Purif. Technol. 323 (2023), 124465.
[34] P. Hu, J. Hu, H. Wang, H. Liu, J. Zhou, Y. Liu, Y. Wang, H. Ji, One-Step Ethylene Purification by an Ethane-Screening Metal-Organic Framework, ACS Appl. Mater. Interfaces 14 (13) (2022) 15195–15204.
[35] M.-H. Yu, H. Fang, H.-L. Huang, M. Zhao, Z.-Y. Su, H.-X. Nie, Z. Chang, T.-L. Hu, Tuning the Trade-Off between Ethane/Ethylene Selectivity and Adsorption Capacity within Isoreticular Microporous Metal−Organic Frameworks by Linker Fine-Fluorination, Small 19 (2023) 2300821.
[36] G.M. Sheldrick, SHELXT - integrated space-group and crystal-structure determination, Acta Cryst. A, 71 (2015), 3-8.
[37] G.M. Sheldrick, Crystal structure refinement with SHELXL, Acta Cryst. C 71 (2015) 3–8.
[38] O.V. Dolomanov, L.J. Bourhis, R.J. Gildea, J.A.K. Howard, & Puschmann, H, J. Appl. Cryst. 42 (2009) 339–341.
[39] A.L. Spek, Single-crystal structure validation with the program PLATON, J. Appl. Cryst. 36 (1) (2003) 7–13.
[40] D.-D. Zhou, C.-T. He, P.-Q. Liao, W. Xue, W.-X. Zhang, H.-L. Zhou, J.-P. Zhang, X.-M. Chen, A Flexible Porous Cu(ii) Bis-imidazolate Framework with Ultrahigh Concentration of Active Sites for Efficient and Recyclable CO2 Capture, Chem. Commun. 49 (2013) 11728–11730.
[41] Y. Wu, H. Chen, D. Liu, Y. Qian, H. Xi, Adsorption and Separation of Ethane/ethylene on ZIFs with Various Topologies: Combining GCMC Simulation with the Ideal Adsorbed Solution Theory (IAST), Chem. Eng. Sci. 124 (2015) 144–153.
[42] F.-Z. Sun, S.-Q. Yang, R. Krishna, Y.-H. Zhang, Y.-P. Xia, T.-L. Hu, Microporous Metal-Organic Framework with a Completely Reversed Adsorption Relationship for C2 Hydrocarbons at Room Temperature, ACS Appl. Mater. Interfaces 12 (2020) 6105–6111.
[43] D. Kim, D. Jo, J.W. Yoon, S.-K. Lee, K.H. Cho, Y.-S. Bae, U.H. Lee, High-Performance Adsorbent for Ethane/Ethylene Separation Selected through the Computational Screening of Aluminum-Based Metal-Organic Frameworks, ACS Appl. Mater. Interfaces 14 (2022) 43637–43645.
[44] Q. Hong, W. Wang, S. Chen, K. Chen, M. Liu, H.-X. Zhang, J. Zhang, Host-Guest Pore Space Partition in a Boron Imidazolate Framework for Ethylene Separation, Chem. Mater. 34 (2022) 307–313.
[45] G.-D. Wang, R. Krishna, Y.-Z. Li, W.-J. Shi, L. Hou, Y.-Y. Wang, Z. Zhu, Boosting Ethane/Ethylene Separation by MOFs through the Amino-Functionalization of Pores, Angew. Chem. Int. Ed. 61 (2023) e202213015.
[46] J.-J. Li, S.-Y. Liu, G. Liu, Y.-G., G.-Z. Wu, H.-D. Li, R. Krishna, X.-Q. Liu, L.-B. Sun, A Robust Perylene Diimide-based Zirconium Metalorganic Framework for Preferential Adsorption of Ethane over Ethylene, Sep. Purif. Technol. 320 (2023) 124109.
[47] Y. Zhou, C. Chen, R. Krishna, Z. Ji, D. Yuan, M. Wu, Tuning Pore Polarization to Boost Ethane/Ethylene Separation Performance in Hydrogen-Bonded Organic Frameworks, Angew. Chem. Int. Ed. 62 (2023) e202305041.

Customized Pore Fluorination in a Microporous Metal-organic Framework for Efficient Ethane/ethylene Separation

Hong-Xiang Nie [a], Mei-Hui Yu [a], Qiang Gao [b] *, Rajamani Krishna [c] and Ze Chang [a] *

[a] School of Materials Science and Engineering, National Institute for Advanced Materials, Nankai University, Tianjin 300350, China.

[b] College of Environmental and Chemical Engineering, Jiangsu University of Science and Technology, Zhenjiang 212100, China.

[c] Van't Hoff Institute for Molecular Sciences, University of Amsterdam, The Netherlands.

General materials and methods

1. Isosteric Heat of Adsorption (Q_{st}) Calculations

The virial-type equation was used to calculate the enthalpies of adsorption for C_2H_2, C_2H_4 at 273 K and 298 K in **NKU-0821a**. At two temperatures, the data were fitted using the equation S1:

$$\boldsymbol{\ln P = \ln N + \frac{1}{T}\sum_{i=0}^{m} a_i N^i + \sum_{j=0}^{n} b_j N^j} \qquad \text{(S1)}$$

Here, P is the pressure in Torr, N is the amount adsorbed in mmol g^{-1}, T is temperature in K, and a_i and b_j are virial coefficients which are temperature independent empirical parameters. Based on the virial coefficients obtained from the fitted isotherms, the isosteric heat of adsorption (Q_{st}) was calculated using the following equation S2:

$$\boldsymbol{Q_{st} = -R\sum_{i=0}^{m} a_i N^i} \qquad \text{(S2)}$$

Q_{st} is the coverage-dependent isosteric heat of adsorption and R is the universal gas constant.

2. Calculation of Selectivity via Ideal Adsorption Solution Theory (IAST)

The experimental isotherm data on pure component for C_2H_2 and C_2H_4 in **NKU-0821a** were measured at temperatures of 273 and 298 K, respectively, which were fitted by dual-site Langmuir–Freundlich model (equation S3):

$$\boldsymbol{q = \frac{q_{A,sat} b_A p^{1/n_1}}{1 + b_A p^{1/n_1}} + \frac{q_{B,sat} b_B p^{1/n_2}}{1 + b_B p^{1/n_2}}} \qquad \text{(S3)}$$

Here, p is the pressure in kPa, q is the adsorbed amount in mmol·g^{-1}, $q_{A,sat}$ and $q_{B,sat}$ are the saturation capacities of sites A and B. b_A and b_B are the affinity coefficients of sites A and B in kPa^{-1}, and n_1 and n_2 represent the deviations from an ideal homogeneous surface. The fitted parameters were used to predict multi-component adsorption with IAST.

The selectivity S_{ads} in a binary mixture of components is defined as equation S4:

$$\boldsymbol{S_{ads} = \frac{q_1/q_2}{p_1/p_2}} \qquad \text{(S4)}$$

In which, q_i represents the amount of i adsorbed and p_i represents the partial pressure

of *i* in the mixture.

3. Transient breakthrough simulations

To match the experimental breakthroughs for binary 50/50 C_2H_6/C_2H_4 mixtures using **NKU-0821a**, simulations were conducted using the set of parameters as in the experiments: inside tube diameter = 10 mm, length of packed tube, L = 120 mm, mass of adsorbent, = 3.28 g, volumetric flow rate of gas mixture at inlet to tube, = 5 mL min^{-1}. The experimental breakthroughs have distended characteristics that can be captured by introducing diffusional influences in the breakthrough simulations using the methodology described by Krishna.[1, 2] To get reasonable match with experiments, the Maxwell-Stefan diffusivities of C_2H_6, and C_2H_4 are taken to be, and , respectively, where is the radius of the MOF crystals packed in the tube.

The breakthrough data are presented in terms of the dimensionless concentrations at the exit of the fixed bed, C_i/C_{i0} , as function of the modified time parameter

$$\frac{(\text{time in s})}{(\text{g MOF packed in tube})} = \frac{t}{m_{ads}} = \text{s g}^{-1}$$

.

Table S1. Crystal data and structure refinement parameters for **NKU-0821**

Empirical formula	$C_{13}H_6FNO_4Zn$
Formula weight (g mol^{-1})	324.56
Crystal system	monoclinic
Space group	$P2_1/n$
CCDC number	2280924
a (Å)	16.4981(2)
b (Å)	23.7983(2)
c (Å)	17.6933(2)
α (°)	90
β (°)	116.6430(10)
γ (°)	90
V ($Å^3$)	6209.23(13)
Z	12
ρ_{calc} (g cm^{-3})	1.042
μ (mm^{-1})	1.807
F (000)	1944.0
Radiation (Å)	Cu Kα (λ = 1.54184)
2Θ range for data collection/°	7.136 to 151.982
Index ranges	-20≤h≤18, -25≤k≤29, -15≤l≤22
Reflections collected	33475
Independent reflections	12420 [R_{int} = 0.0323, R_{sigma} = 0.0360]
Data/restraints/parameters	12420/0/542
Goodness-of-fit on F^2	1.076
Final R indexes [I >= 2σ (I)][a]	R_1 = 0.0473, wR_2 =0.1367
Final R indexes [all data][b]	R_1 = 0.0530, wR_2 = 0.1396
Largest diff. peak/hole / e $Å^{-3}$	0.92/-0.65

[a] $R_1=\sum||F_o| - |F_c||/\sum|F_o|$. [b] $wR_2=\{\sum[w(F_o^2 - F_c^2)^2]/\sum w(F_o^2)^2\}^{1/2}$

Table S2. Comparison of C_2H_6 uptake and Q_{st} for **NKU-0821a** and other MOFs

MOFs	C_2H_6 uptake (mmol g^{-1})	Q_{st} of C_2H_6 (kJ mol^{-1})	References
UiO-67-$(NH_2)_2$	4.32	26.5	[3]
UiO-67-BN	3.9	24.6	[4]
NUM-7	2.85	35.8	[5]
Cu(Qc)$_2$	1.85	28.8	[6]
$Fe_2(O_2)$(dobdc)	3.03	66.8	[7]
LIFM-63	2.89	26.5	[6]
CAU-11	1.81	31.0	[8]
$Zn_2(oba)_2$(dmimpym)	2.52	26.5	[9]
ZUL-C3	2.30	29.5	[10]
ZUL-C4	2.93	31.6	[10]
BIF-108-Zn	2.8	22.5	[11]
NKMOF-8-Me	4.67	38.4	[12]
Tb-MOF-76(NH_2)	3.04	32.8	[13]
Zr-Me-PDI	3.9	≈16.5	[14]
HOF-NBDA	3.98	23.5	[15]
NKU-0821a	4.3	25.3	**This work**

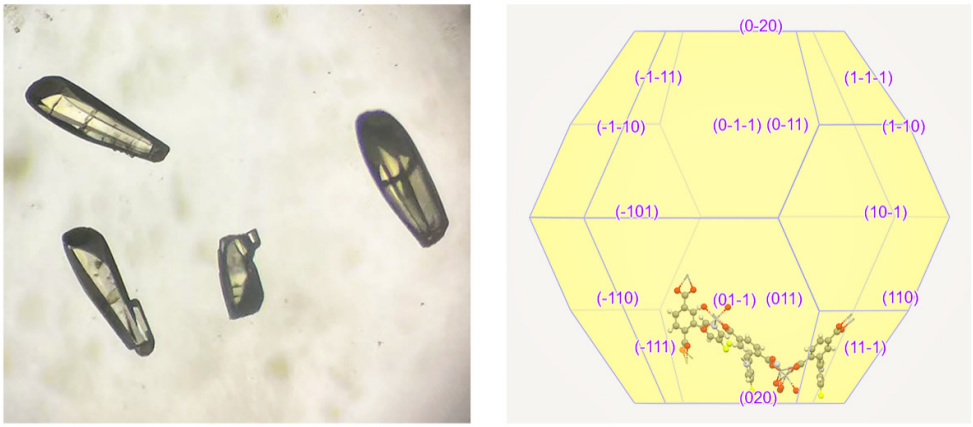

Figure S1. Optical microscope image of **NKU-0821**.

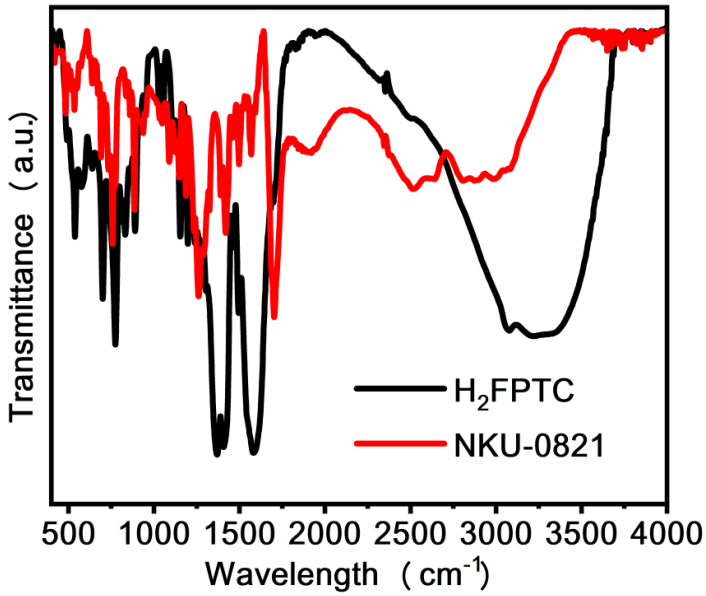

Figure S2. Comparison of FTIR spectra of as-synthesized **NKU-0821** and ligand.

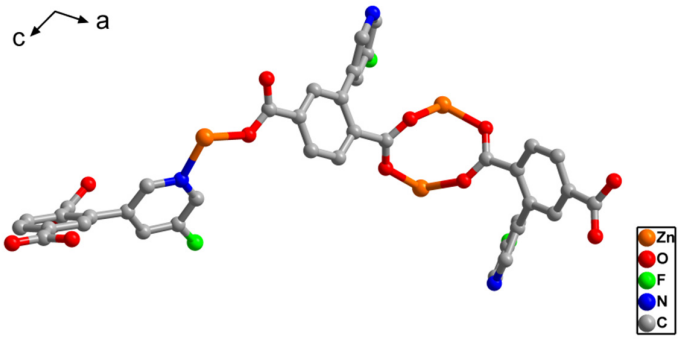

Figure S3. The asymmetric unit for **NKU-0821** (hydrogen atoms were omitted).

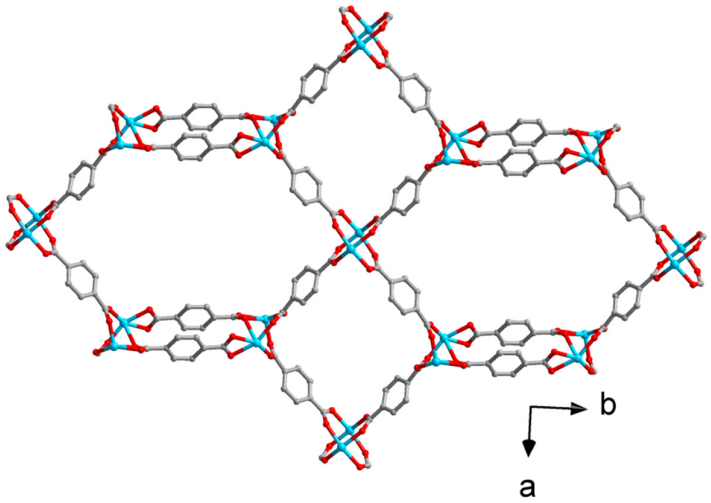

Figure S4. The asymmetric unit for **NKU-0821** (hydrogen atoms were omitted).

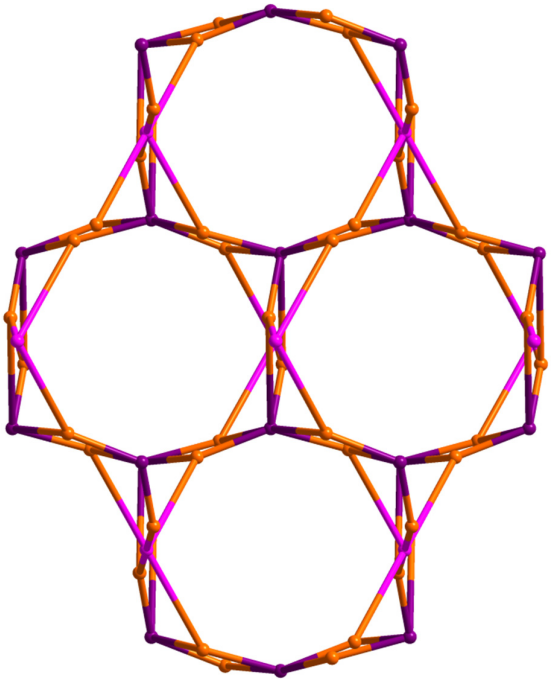

Figure S5. The topology simplification of **NKU-0821.**

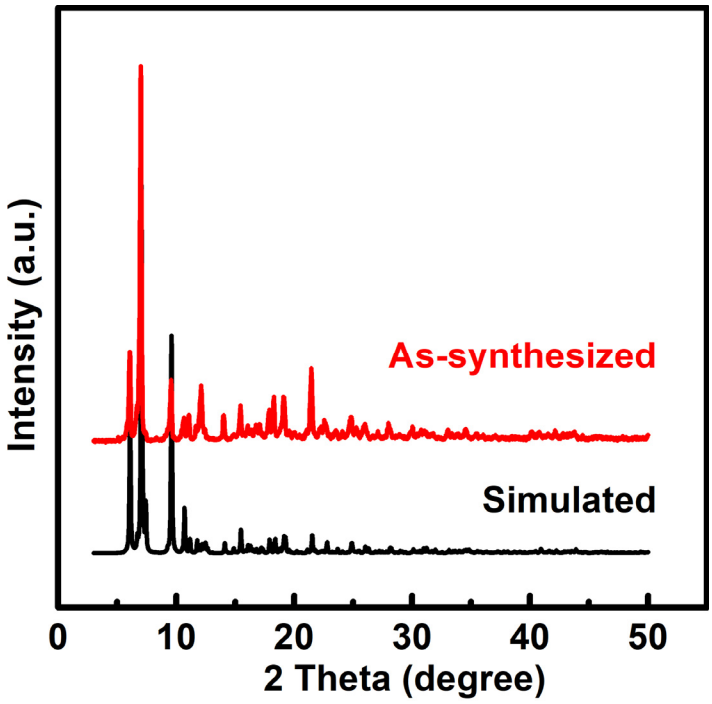

Figure S6. The PXRD patterns of the simulated and as-synthesized **NKU-0821**.

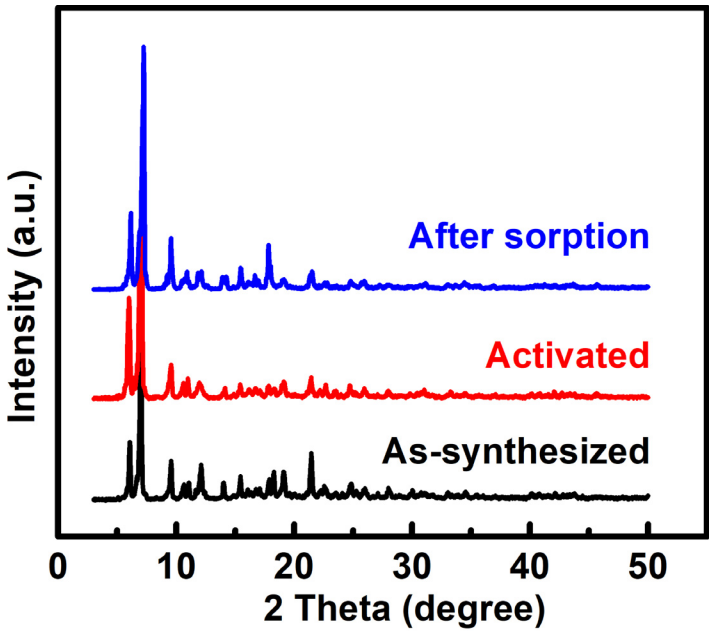

Figure S7. The PXRD patterns of the as-synthesized, activated, after sorption **NKU-0821**.

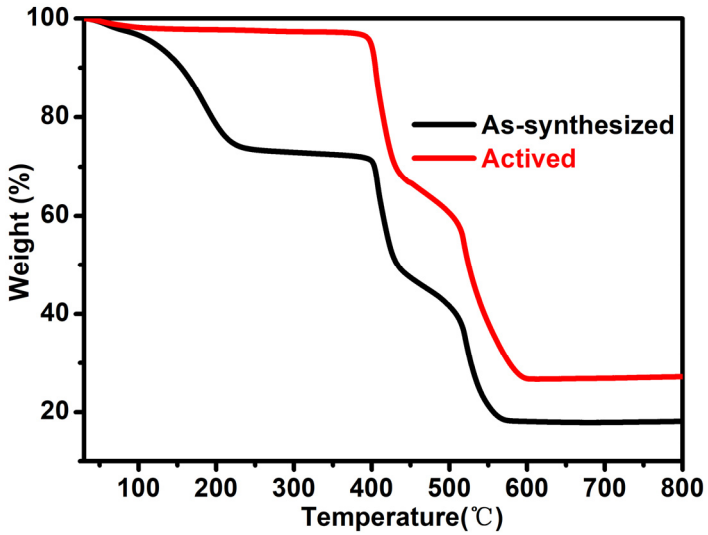

Figure S8. The PXRD patterns of the as-synthesized and activated **NKU-0821.**

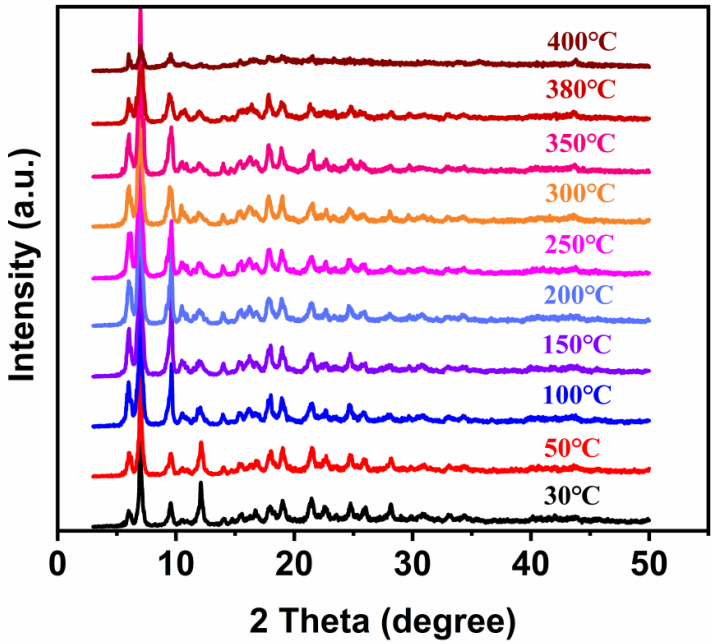

Figure S9. The VT-PXRD patterns of the as-synthesized **NKU-0821.**

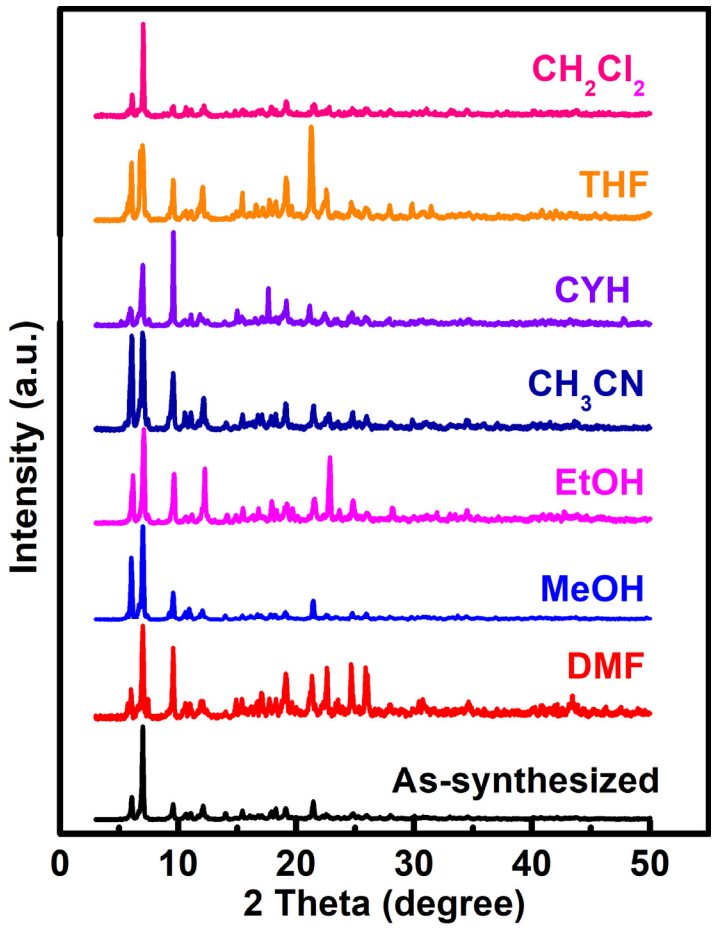

Figure S10. The PXRD patterns for **NKU-0821** after exposure in common solvents.

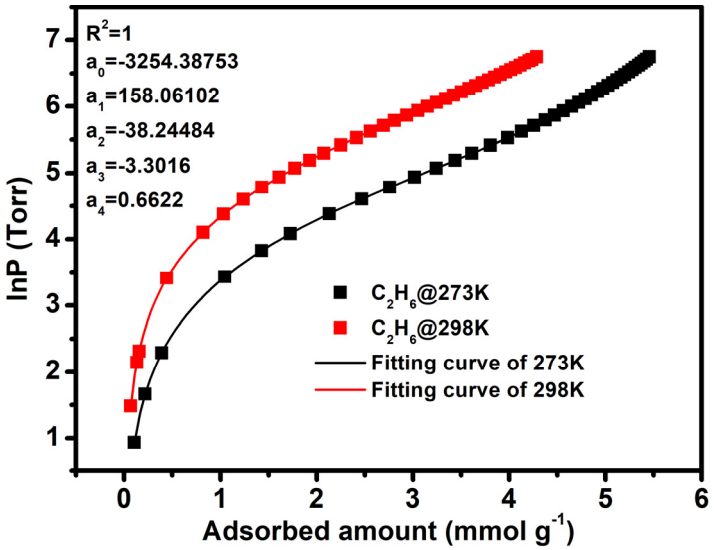

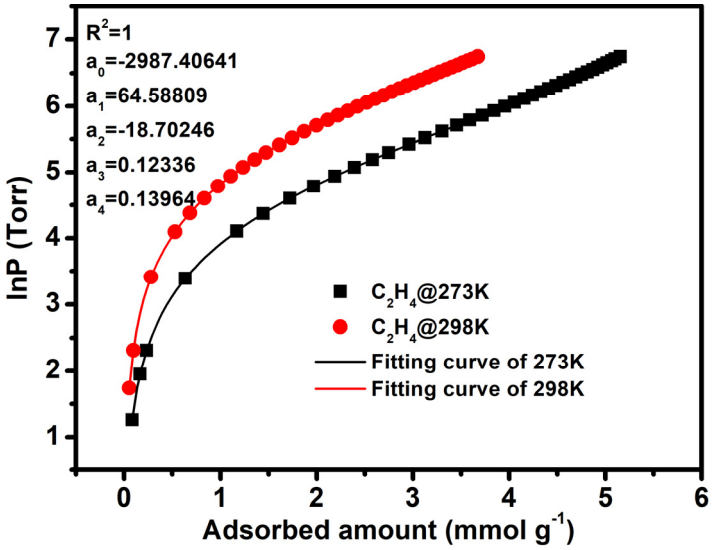

Figure S11. The details of virial equation (solid lines) fitting to the experimental C_2H_6 and C_2H_4 adsorption data (symbols) for **NKU-0821a**.

Table S3. The fitting parameter of virial equation.

Fitting parameter	C_2H_6	C_2H_4
a_0	-3254.38753	-2928.40641
a_1	158.06102	64.58809
a_2	-38.24484	-18.70246
a_3	-3.3016	0.12336
a_4	0.6622	0.13964
b_0	15.06141	14.66017
b_1	-0.35564	-0.03895
b_2	0.15689	0.06646

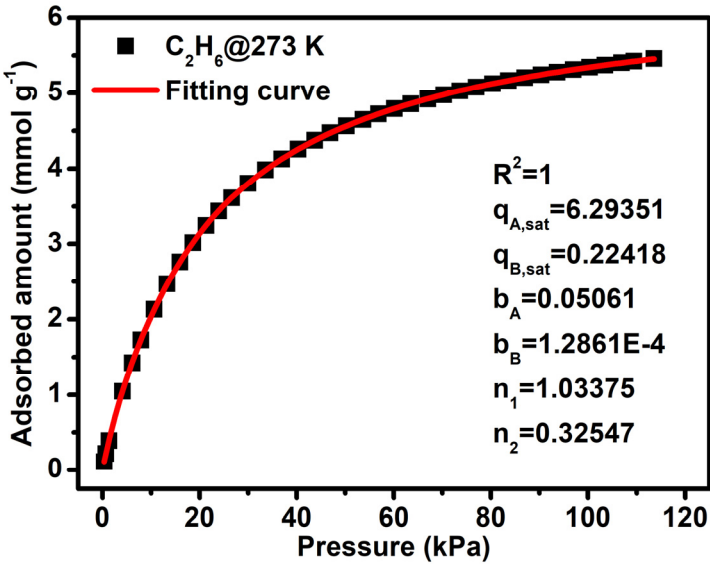

Figure S12. The details of dual-Langmuir-Freundlich isotherm (solid lines) fitting to the experimental C_2H_6 adsorption data (symbols) for **NKU-0821a** at 273 K.

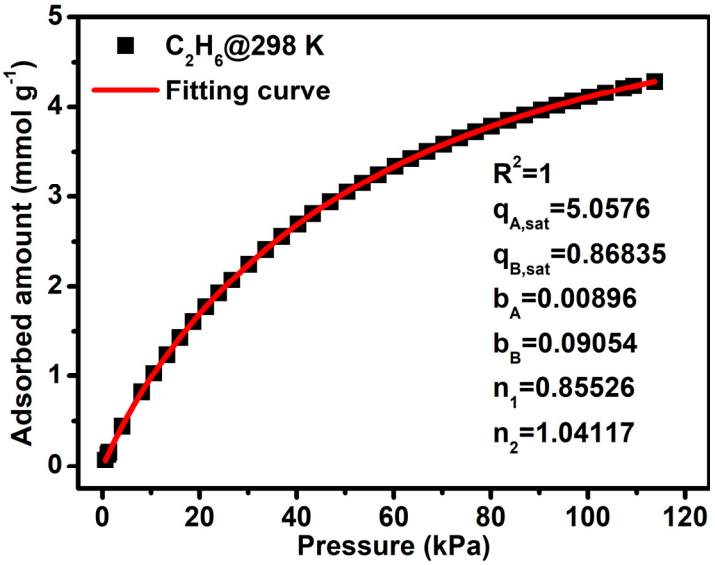

Figure S13. The details of dual-Langmuir-Freundlich isotherm (solid lines) fitting to the experimental C_2H_6 adsorption data (symbols) for **NKU-0821a** at 298 K.

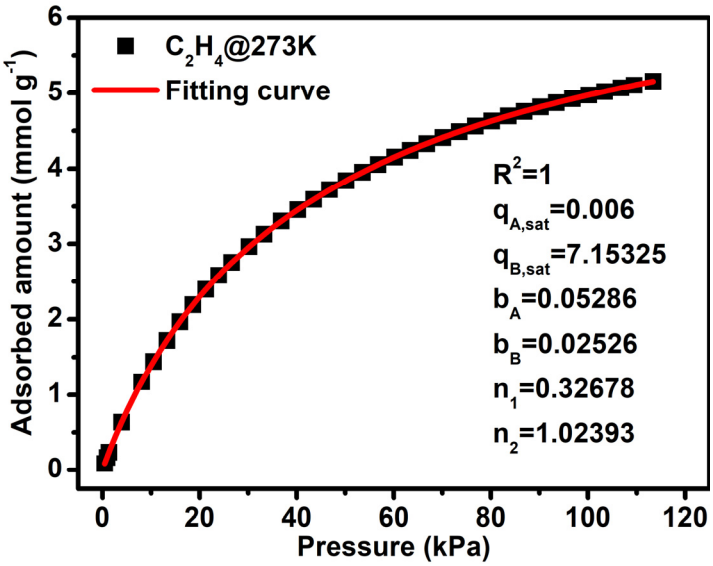

Figure S14. The details of dual-Langmuir-Freundlich isotherm (solid lines) fitting to the experimental C_2H_4 adsorption data (symbols) for **NKU-0821a** at 273 K.

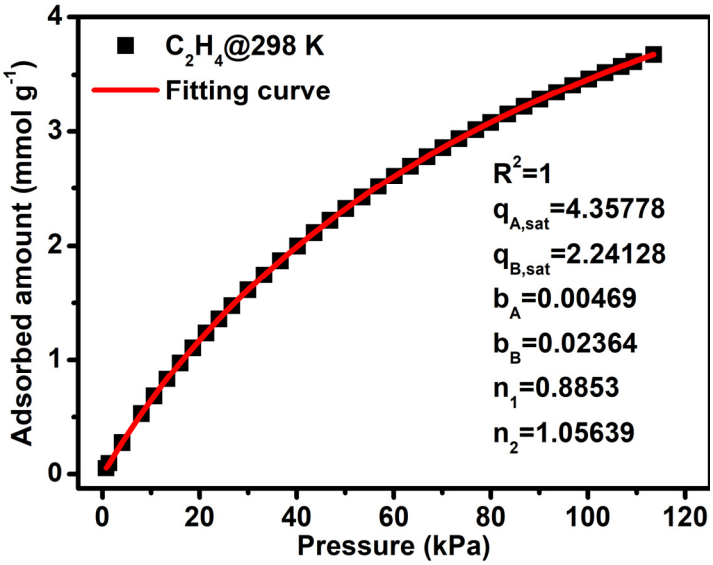

Figure S15. The details of dual-Langmuir-Freundlich isotherm (solid lines) fitting to the experimental C_2H_4 adsorption data (symbols) for **NKU-0821a** at 298 K.

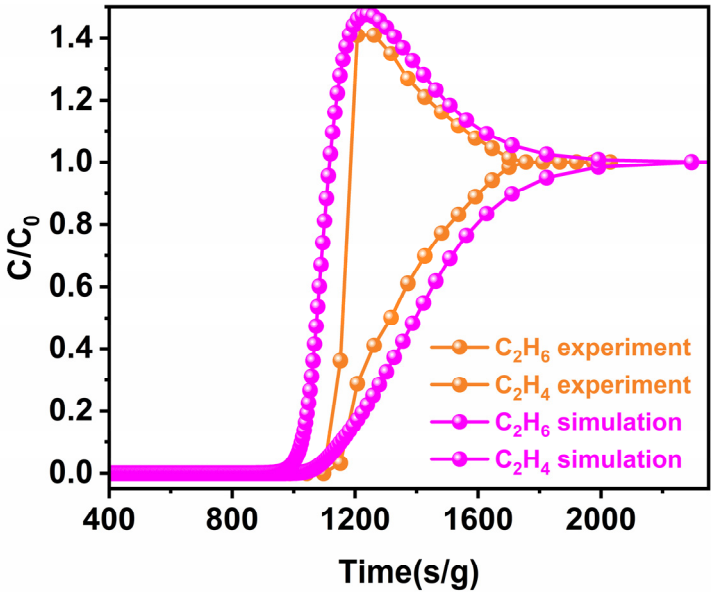

Figure S16. Experimental breakthroughs vs simulations for **NKU-0821a**

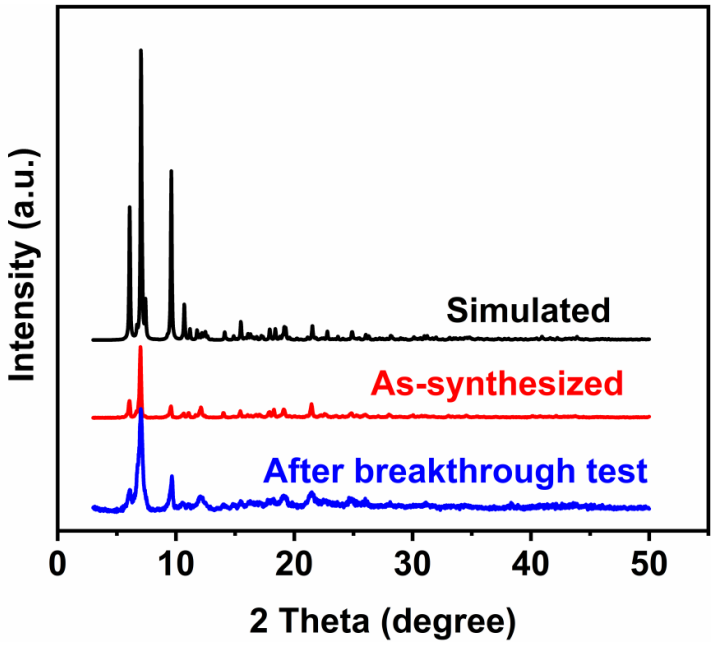

Figure S17. PXRD comparison of **NKU-0821a** after breakthrough test with synthetic and simulated **NKU-0821**.

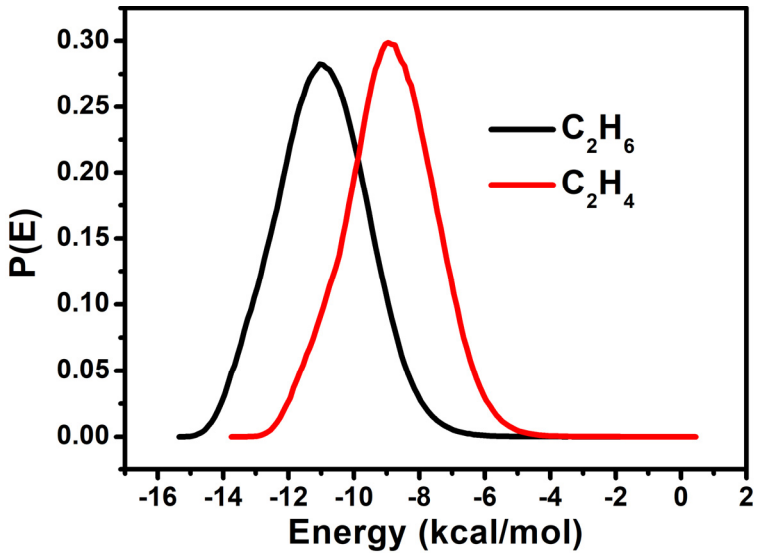

Figure S18. Isosteric heats of C_2H_6 and C_2H_4 in **NKU-0821a**.

References

[1] Krishna, R. Metrics for Evaluation and Screening of Metal-Organic Frameworks for Applications in Mixture Separations. ACS Omega 2020, 5 (2020), 16987−17004.
[2] Krishna, R. Methodologies for Evaluation of Metal-Organic Frameworks in Separation Applications. RSC Advances, 5 (2015), 52269-52295
[3] X.-W. Gu, J.-X. Wang, E. Wu, H. Wu, W. Zhou, G. Qian, B. Chen, B. Li, Immobilization of Lewis Basic Sites into a Stable Ethane-Selective MOF Enabling One-step Separation of Ethylene from a Ternary Mixture, Journal of the American Chemical Society, 144 (2022) 2614-2623.
[4] Y. Han, L. Meng, Y. Liu, H. Li, Z. Ji, Y. Zhou, M. Wu, Z. Han, Expanding Nonpolar Pore Surfaces in Stable Ethane-selective MOF to Boost Ethane/Ethylene Separation Performance, Separation and Purification Technology, 315 (2023) 123642.
[5] F.-Z. Sun, S.-Q. Yang, R. Krishna, Y.-H. Zhang, Y.-P. Xia, T.-L. Hu, Microporous Metal–Organic Framework with a Completely Reversed Adsorption Relationship for C2 Hydrocarbons at Room Temperature, ACS Applied Materials & Interfaces, 12 (2020) 6105-6111.
[6] R.-B. Lin, H. Wu, L. Li, X.-L. Tang, Z. Li, J. Gao, H. Cui, W. Zhou, B. Chen, Boosting Ethane/Ethylene Separation within Isoreticular Ultramicroporous Metal–Organic Frameworks, Journal of the American Chemical Society, 140 (2018) 12940-12946.
[7] L. Li, R.-B. Lin, R. Krishna, H. Li, S. Xiang, H. Wu, J. Li, W. Zhou, B. Chen, Ethane/Ethylene Separation in a Metal-organic Framework with Iron-peroxo Sites, Science, 362 (2018) 443-446.
[8] D. Kim, D. Jo, J.W. Yoon, S.-K. Lee, K.H. Cho, Y.-S. Bae, U.H. Lee, High-Performance Adsorbent for Ethane/Ethylene Separation Selected through the Computational Screening of Aluminum-Based Metal–Organic Frameworks, ACS Applied Materials & Interfaces, 14 (2022) 43637-43645.
[9] Y.-Z. Li, G.-D. Wang, R. Krishna, Q. Yin, D. Zhao, J. Qi, Y. Sui, L. Hou, A separation MOF with O/N active sites in nonpolar pore for One-step C_2H_4 purification from C_2H_6 or C_3H_6 mixtures, Chemical Engineering Journal, 466 (2023) 143056.
[10] J. Zhou, T. Ke, X. Zhu, B. Jin, Z. Bao, Z. Zhang, Y. Yang, Q. Ren, Q. Yang, Combination of Low-Polar and Polar Binding Sites in Aliphatic MOFs for the Efficient C_2H_6/C_2H_4 Separation, ACS Applied Materials & Interfaces, 15 (2023) 3387-3394.
[11] Q. Hong, W. Wang, S. Chen, K. Chen, M. Liu, H.-X. Zhang, J. Zhang, Host–Guest Pore Space Partition in a Boron Imidazolate Framework for Ethylene Separation, Chemistry of Materials, 34 (2022) 307-313.
[12] S. Geng, E. Lin, X. Li, W. Liu, T. Wang, Z. Wang, D. Sensharma, S. Darwish, Y.H. Andaloussi, T. Pham, P. Cheng, M.J. Zaworotko, Y. Chen, Z. Zhang, Scalable Room-Temperature Synthesis of Highly Robust Ethane-Selective Metal–Organic Frameworks for Efficient Ethylene Purification, Journal of the American Chemical Society, 143 (2021) 8654-8660.
[13] G.-D. Wang, R. Krishna, Y.-Z. Li, W.-J. Shi, L. Hou, Y.-Y. Wang, Z. Zhu, Boosting Ethane/Ethylene Separation by MOFs through the Amino-Functionalization of Pores,

Angewandte Chemie International Edition, 61 (2023) e202213015.
[14] J.-J. Li, S.-Y. Liu, G. Liu, Y.-G., G.-Z. Wu, H.-D. Li, R. Krishna, X.-Q. Liu, L.-B. Sun, A Robust Perylene Diimide-based Zirconium Metalorganic Framework for Preferential Adsorption of Ethane over Ethylene, Separation and Purification Technology, 320 (2023) 124109.
[15] Y. Zhou, C. Chen, R. Krishna, Z. Ji, D. Yuan, M. Wu, Tuning Pore Polarization to Boost Ethane/Ethylene Separation Performance in Hydrogen-Bonded Organic Frameworks, Angewandte Chemie International Edition, 62 (2023) e202305041.